Simultaneous nanostructure and chemical imaging of intact whole nematodes

Michael W.M. Jones [abc*+], Nicholas W. Phillips [cd+], Brian Abbey [de], Dominic J. Hare [f], Grant A. van Riessen [e], David J. Vine [g], Martin D. de Jonge [b], Gawain McColl [f]

[a] Central Analytical Research Facility, Institute of Future Environments, Queensland University of Technology, Brisbane, Queensland 4000, Australia.
[b] Australian Synchrotron, 800 Blackburn Road, Clayton, Victoria 3168, Australia.
[c] ARC Centre of Excellence in Advanced Molecular Imaging, La Trobe Institute for Molecular Sciences, La Trobe University, Victoria 3086, Australia.
[d] Department of Engineering Science, University of Oxford, Oxford, Oxfordshire OX1 3PJ, UK.
[e] Department of Chemistry and Physics, La Trobe Institute for Molecular Science, La Trobe University, Victoria 3086, Australia.
[f] The Florey Institute of Neuroscience and Mental Health, The University of Melbourne, Parkville, Victoria, 3052, Australia.
[g] X-ray Science Division, Advanced Photon Source, Argonne National Laboratory, Argonne, IL 60439, USA.
[+] these authors contributed equally
*Correspondence e-mail: mw.jones@qut.edu.au

Methods

Caenorhabditis elegans, strain CL2122[1] [*dvIs15*(*mtl-2*:*gfp*)], cultured under standard conditions[2] at 20 °C were split into two populations at the forth larval stage (L4), and cultured on nematode growth agar media with or without 100 µM $CuCl_2$. Following 24 hours exposure at 20 °C samples were isolated, washed and freeze dried on silicon nitride windows as described in reference [3] and placed at the 2.5 µm FWHM focused 10 keV X-rays of a KB mirror pair. The *C. elegans* specimens were scanned in the focal plane of the KB mirrors in both the horizontal and vertical directions with sampling intervals in both axes of 400 nm as described in reference[4]. The horizontal axis was scanned 'on-the-fly' at 20 μms^{-1}, resulting in a data collection rate of 6.7 $\mu m^2 s^{-1}$ including end-of-line overheads. Up to 511,000 diffraction frames (188,000 to 511,000 diffraction frames with areas of between 0.045 and 0.082 mm^2) were collected for each specimen using an EIGER X 1M detector with 75 µm square pixels, placed 3.67 m downstream of the focus. Using an event-mode data acquisition scheme[4]. Fluorescence data was collected simultaneously using a 384-element Maia (Revision C) detector[5] placed in its usual backscatter geometry. For a rigorous explanation of the method used to collect ptychography data at the XFM beamline of The Australian Synchrotron the reader should refer to the prior publication of Jones *et al.*[4], of which the data was collected under the same conditions to that which is presented here. The total dose (equal to the dose for fluorescence imaging) received by each specimen was approximately 8.5×10^4 Gy and 1.5×10^4 Gy for the fly and step scans respectively due to dose accumulated during stage moves associated with step scanning, while the ptychography imaging dose for each case was 4.3×10^4 Gy and 7.7×10^4 Gy respectively with differences arising from different sampling densities.

Diffraction patterns were cropped to 128 × 128 pixels centred on the diffraction pattern yielding a reconstructed ptychography pixel size equal to 47.4 nm. Each diffraction dataset was split into overlapping subsets of approximately 64000 diffraction frames as shown in Fig. 1 equating to approximately 22 min of data acquisition time. Each subset was reconstructed on a single node with two GPUs (NVIDIA M2070) on the Multi-modal Australian ScienceS Imaging and Visualisation Environment (MASSIVE)[6] with the ePIE algorithm[7] for 500 iterations with 10 orthogonal probe modes, initially assumed to be a Gaussian with 2.5 µm FWHM[8]. Splitting the dataset into overlapping subsets across many compute nodes offers several advantages; firstly, it allows parallel processing of the entire dataset (in this case, up to 17 compute nodes were used for a single dataset), and secondly, as the data was collected over a significant time, splitting the dataset into smaller subsets allows the effective imaging time for each reconstruction to be significantly reduced, effectively eliminating the adverse effects of an evolving probe in time. As the algorithm does not constrain the phase, the residual background phase gradient and offset was removed with a rolling ball background subtraction with a radius of 4000 pixels in ImageJ to ensure a smooth background was subtracted [4]. Once the background was subtracted, the images were recombined using a globally optimal image stitching method as implemented in the Stitching Plugin[9] in Fiji[10]. The validity of this approach is independent of the specific reconstruction code used in recovering the phase. Fluorescence data was analysed using the dynamic array method in GeoPIXE[11], with elemental maps generated as quantitative 32 bit images.
Registration of the XFM images to the ptychography images consisted of resizing the XFM images using bicubic interpolation using Fiji[10] to the same physical pixel size (~47.7nm), before the Compton scatter image was aligned to the ptychography image using a multimodal rigid transformation using the Matlab® function imregtform[12]. The results of the alignment were visually confirmed before the same set of transformations were then applied to all other elemental maps. Segmentation was done visually in Fiji[10] using the ptychography image. The selected region was then used to measure mean elemental abundance and standard deviation in each region.

Complete Datasets

Figures S1-S5 show the ptychography phase (a) overlaid with elemental calcium (b) and copper (c). Compared to the phase reconstructed through ptychography, Compton scatter (d) gives low resolution representation of the ultrastructure. The

reconstructed probe for each subregion of ptychographic reconstruction are shown in (e), highlighting variabilities in the incident probe for each case. The probe modes show similar structure to the probe recovered by Jones *et al.*,[4] under the same experimental conditions and have here been aligned to assist visualisation of the probe evolution. The scale bars in (a) and (e) are equal to 20 μm and 1 μm respectively, while the minimum and maximum values in (a) are in radians, and in (b-d) in μgcm^{-2} according to the colour bars (a-d). The magnitude and phase of the reconstructed probes are encoded according to the colour wheel, where the brightness represents the magnitude and the phase is represented by the colour.

Probe Evolution

It is well established that the probe recovered through a simultaneous reconstruction of the object and the probe contains not only information regarding the incident illumination, but also information relating to the motion of the specimen[4, 14-17]. Horizontal and vertical repetition of the illuminating probe – typically around 1-2 μm FWHM horizontal and 2 μm vertical – is observed with a periodicity approximately equal to the distance between diffraction data acquisitions. The variability of these repetitions may arise from variability in the motion system[4], and accounts for the bulk of the variation in the reconstructed probe.

Each subregion was reconstructed with its own probe. For the step scan (Fig. S1) the reconstructed probe represents approximately 100 minutes of data collection, with the size of each subregion limited by the evolution of the probe. For the fly-scan data (Figs. S2-S5), the subarea size is limited by computational efficiency to approximately 20 minutes of data collection. As a result, the reconstructed probes in Fig. S1 show higher variability that those in Figs. S2-S5.

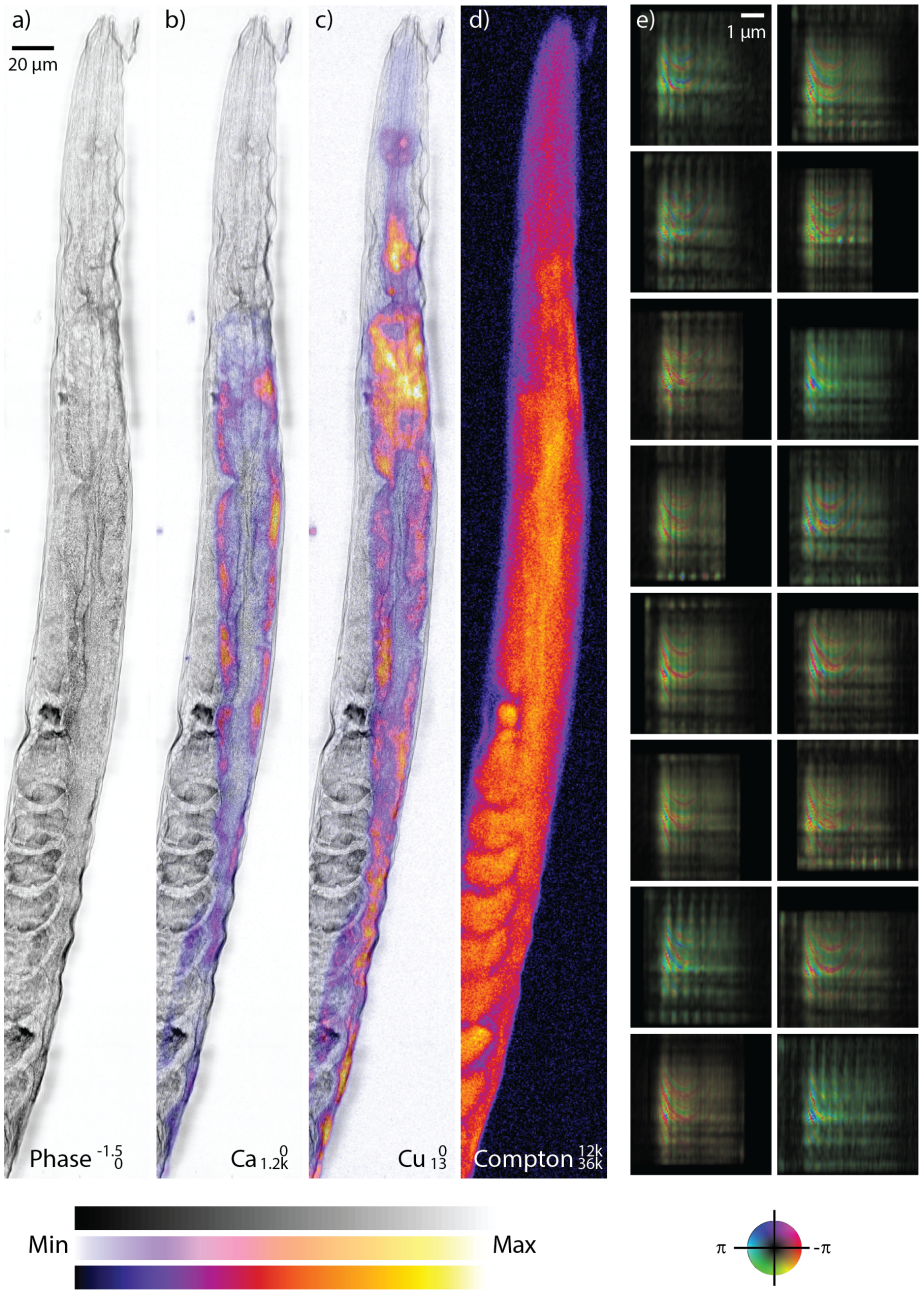

Fig. S1: Ptychography phase (a) overlaid with elemental calcium (b) and copper (c) from a specimen with copper supplementation collected as a step-scan. Compton scatter gives low resolution representation of the ultrastructure (d). The recovered probe for each subregion of ptychographic reconstruction is shown in (e), highlighting variabilities in the reconstructed probe. The scale bars in (a) and (e) are equal to 20 µm and 1 µm respectively, while the minimum and maximum values in (a) are in radians, and in (b-d) in μgcm^{-2} according to the colour bars (a-d). The magnitude and phase of the reconstructed probes are encoded according to the colour wheel, where the brightness represents the magnitude and the phase is represented by the colour. The recovered probes show similar structure to the probe recovered by Jones et al., [4] under the same experimental conditions and have been aligned to highlight variations in the phase and magnitude.

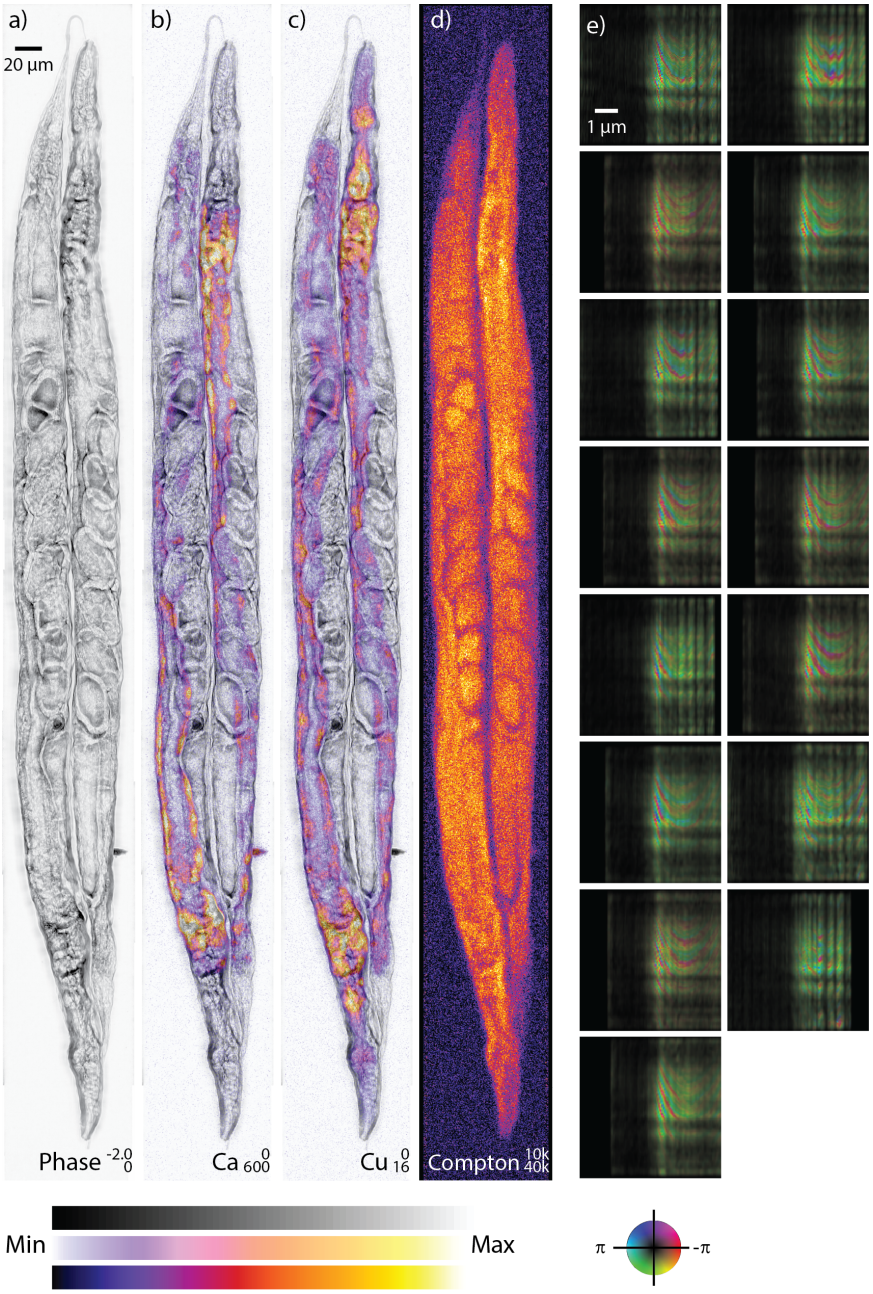

Fig. S2: Ptychography phase (a) overlaid with elemental calcium (b) and copper (c) from a specimen with copper supplementation collected as a fly-scan. Compton scatter gives low resolution representation of the ultrastructure (d). The recovered probe for each subregion of ptychographic reconstruction is shown in (e), highlighting variabilities in the reconstructed probe. The scale bars in (a) and (e) are equal to 20 µm and 1 µm respectively, while the minimum and maximum values in (a) are in radians, and in (b-d) in μgcm^{-2} according to the colour bars (a-d). The magnitude and phase of the reconstructed probes are encoded according to the colour wheel, where the brightness represents the magnitude and the phase is represented by the colour. The probe modes show similar structure to the probe recovered by Jones et al., [4] under the same experimental conditions and have been aligned to highlight variations in the phase and magnitude.

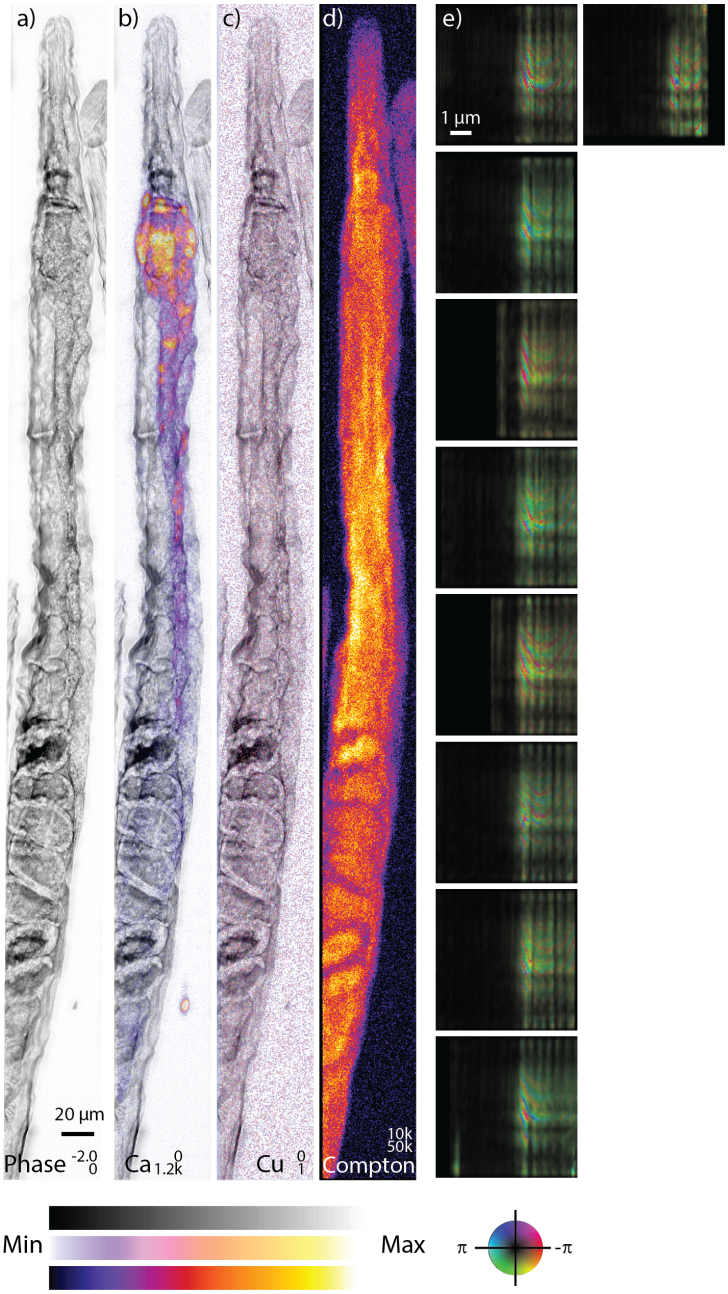

Fig. S3: Ptychography phase (a) overlaid with elemental calcium (b) and copper (c) from a specimen without copper supplementation collected as a fly-scan. Compton scatter gives low resolution representation of the ultrastructure (d). The recovered probe for each subregion of ptychographic reconstruction is shown in (e), highlighting variabilities in the reconstructed probe. The scale bars in (a) and (e) are equal to 20 µm and 1 µm respectively, while the minimum and maximum values in (a) are in radians, and in (b-d) in μgcm^{-2} according to the colour bars (a-d). The magnitude and phase of the reconstructed probes are encoded according to the colour wheel, where the brightness represents the magnitude and the phase is represented by the colour. The probe modes show similar structure to the probe recovered by Jones et al., [4] under the same experimental conditions and have been aligned to highlight variations in the phase and magnitude. At high resolution, the specimen shows the effects of shrinkage during freeze drying.

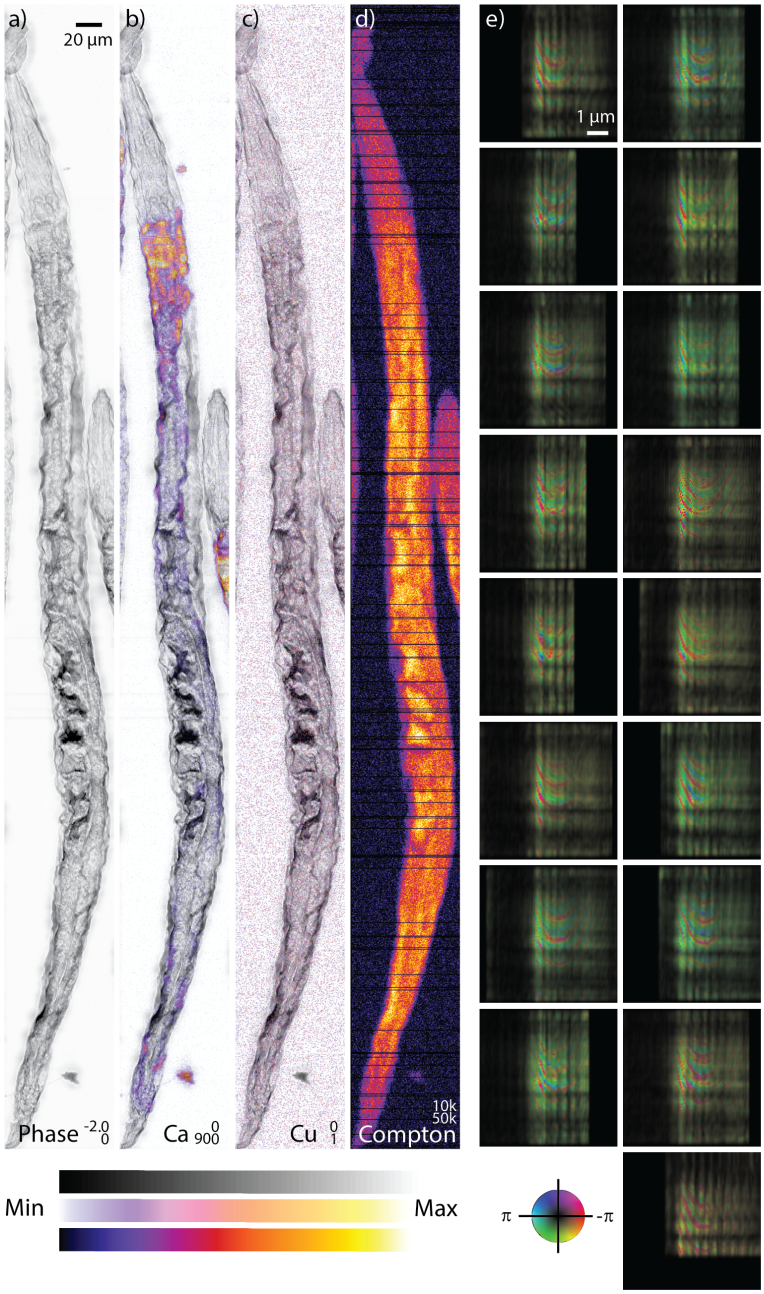

Fig. S4: Ptychography phase (a) overlaid with elemental calcium (b) and copper (c) from a specimen without copper supplementation collected as a fly-scan. Compton scatter gives low resolution representation of the ultrastructure (d). The recovered probe for each subregion of ptychographic reconstruction is shown in (e), highlighting variabilities in the reconstructed probe. The scale bars in (a) and (e) are equal to 20 µm and 1 µm respectively, while the minimum and maximum values in (a) are in radians, and in (b-d) in μgcm^{-2} according to the colour bars (a-d). The magnitude and phase of the reconstructed probes are encoded according to the colour wheel, where the brightness represents the magnitude and the phase is represented by the colour. The probe modes show similar structure to the probe recovered by Jones et al., [4] under the same experimental conditions and have been aligned to highlight variations in the phase and magnitude. Missing lines due to scan errors are evident in the Compton scatter (d) and present in all fluorescence data. The missing lines are not visible in the ptychography image (a) due to the significant overlap between lines. At high resolution, the specimen shows the effects of shrinkage during freeze drying.

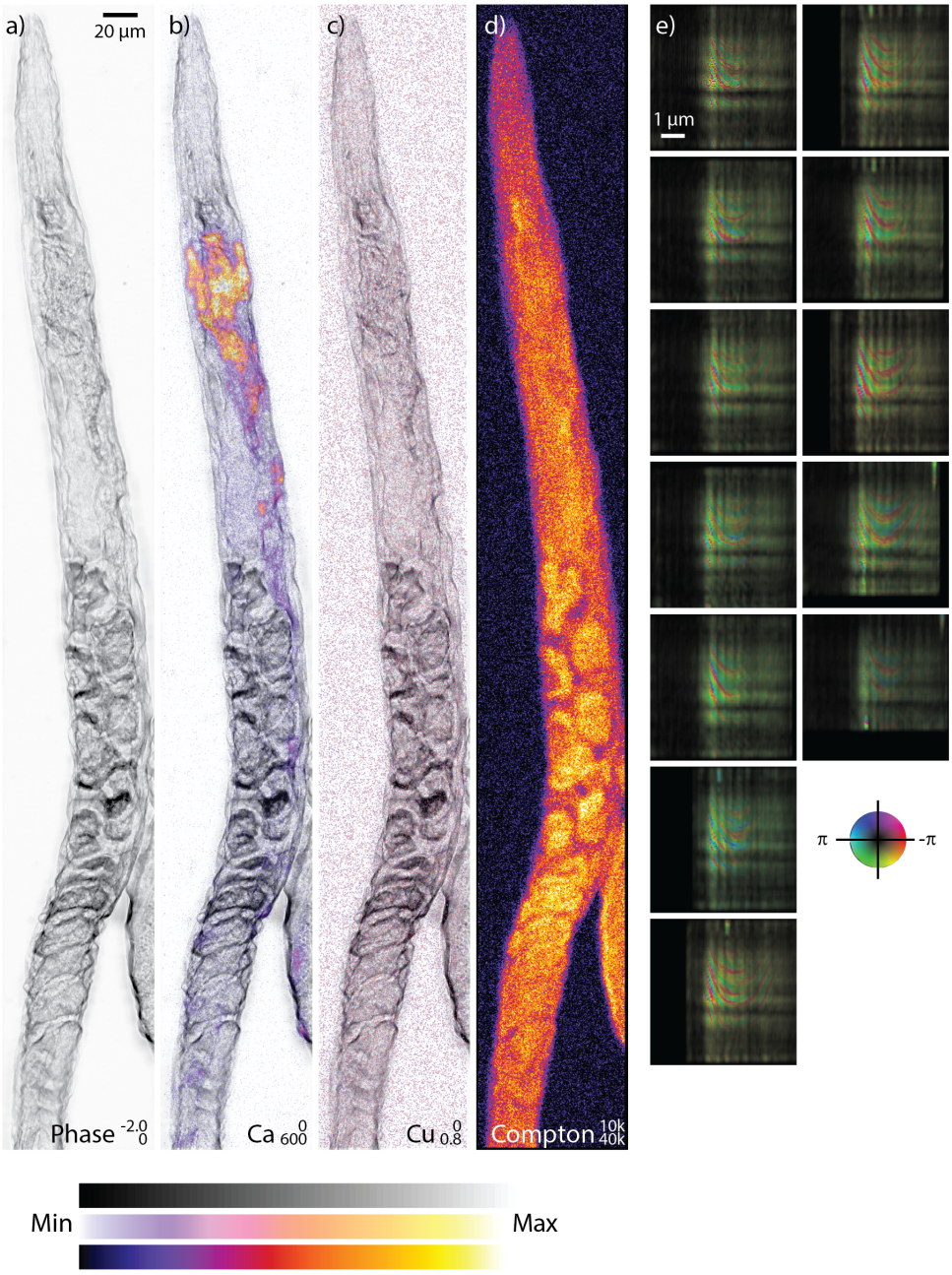

Fig. S5: Ptychography phase (a) overlaid with elemental calcium (b) and copper (c) from a specimen without copper supplementation collected as a fly-scan. Compton scatter gives low resolution representation of the ultrastructure (d). The recovered probe for each subregion of ptychographic reconstruction is shown in (e), highlighting variabilities in the reconstructed probe. The scale bars in (a) and (e) are equal to 20 µm and 1 µm respectively, while the minimum and maximum values in (a) are in radians, and in (b-d) in μgcm^{-2} according to the colour bars (a-d). The magnitude and phase of the reconstructed probes are encoded according to the colour wheel, where the brightness represents the magnitude and the phase is represented by the colour. The probe modes show similar structure to the probe recovered by Jones et al., [4] under the same experimental conditions and have been aligned to highlight variations in the phase and magnitude. At high resolution, the specimen shows the effects of shrinkage during freeze drying.

Reconstructed ptychography image resolution

A Fourier Ring Correlation (FRC)[13] compares the information from two independent ptychography reconstructions to obtain an estimate of the resolution. In this case, the overlapping areas of adjacent sub-sections was used in the FRC. The overlapping regions account for over 85% of the total image area. The FRC is shown with the ½ bit threshold in Figure S1, suggesting a resolution of approximately 280 nm.

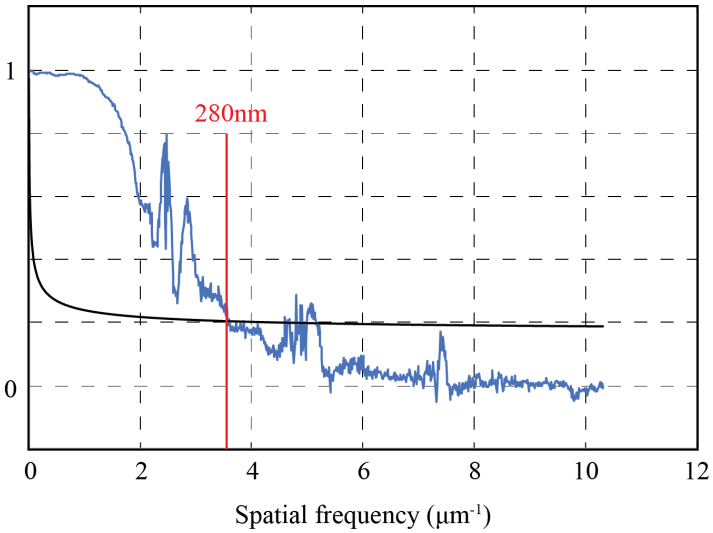

Figure S6: Fourier Ring Correlation analysis of the ptychography data presented in Figure 1. The solid line depicts the ½ bit threshold, which intersects with the reconstructed data at a real space resolution of 280 nm.

Ptychography based segmentation

Figure S7 shows the segmented pharynx of each specimen (red) overlaid on the ptychography image. As shown in Fig. 3b and 3c, the pharynx and its subregions can be reliably segmented based on the ptychography images, where the same regions are indistinct in the Compton scatter images. Figures S2-S6 show that the pharynx is less easily identified by the elemental distributions of the other elemental analytes, apart from copper when animals were supplemented with $CuCl_2$.

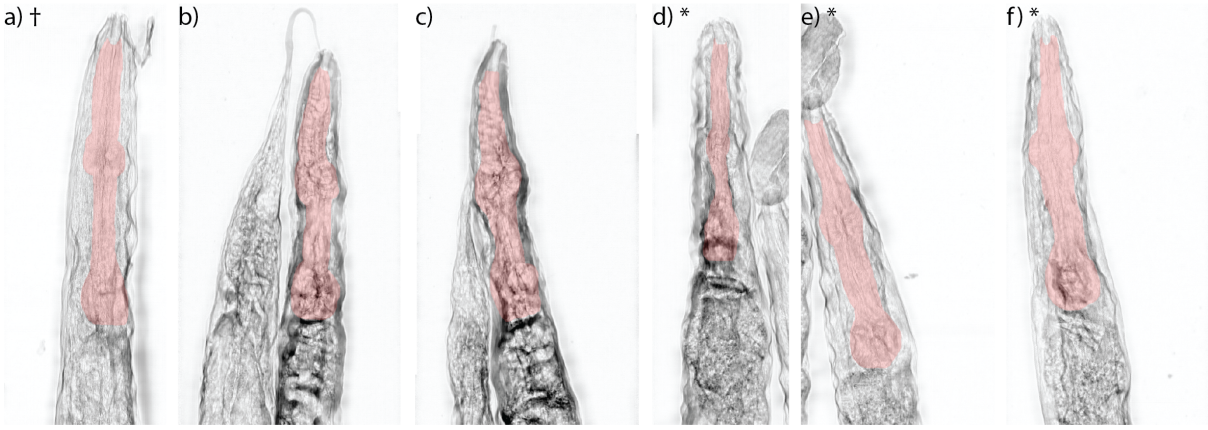

Fig. S7: The pharynx and its subsections are readily identifiable in the ptychography images despite being indistinguishable in the fluorescence images. † denotes a step-scan, while * denotes a specimen without copper supplementation. The complete data for each panel is presented previously as follows: (a) – Fig. S1; (b-c) – Fig. S2; (d) – Fig. S3; (e) – Fig. S4; and (f) – Fig. S5.

Table S1: Area of the segmented features as presented in Fig. 3d. Specimens are as labelled in Fig S7.

	Area (μm^2)					
Specimen	**a)**	**b)**	**c)**	**d)**	**e)**	**f)**
Precorpus	477	424	372	271	331	420
Metacorpus	306	288	372	206	439	392
Isthmus	388	351	232	109	316	501
Terminal Bulb	464	419	165	522	482	616

References

1. D. S. Fay, A. Fluet, C. J. Johnson and C. D. Link, *Journal of Neurochemistry*, 1998, **71**, 1616-1625.
2. S. Brenner, *Genetics*, 1974, **77**, 71-94.
3. D. J. Hare, M. W. M. Jones, V. C. Wimmer, N. L. Jenkins, M. D. de Jonge, A. I. Bush and G. McColl, *Metallomics : integrated biometal science*, 2016, **8**, 156-160.
4. M. W. M. Jones, N. W. Phillips, G. A. van Riessen, B. Abbey, D. J. Vine, Y. S. G. Nashed, S. T. Mudie, N. Afshar, R. Kirkham, B. Chen, E. Balaur and M. D. de Jonge, *Journal of Synchrotron Radiation*, 2016, **23**, 1-7.
5. D. P. Siddons, R. Kirkham, C. G. Ryan, G. De Geronimo, A. Dragone, A. J. Kuczewski, Z. Y. Li, G. A. Carini, D. Pineli, R. Beuttenmuller, D. Elliot, M. Pfeffer, T. A. Tyson, G. F. Moorhead and P. A. Dunn, *Journal of Physics: Conference Series*, 2014, **499**, 012001.
6. W. J. Goscinski, P. McIntosh, U. C. Felzmann, A. Maksimenko, C. J. Hall, T. Gureyev, D. Thompson, A. Janke, G. Galloway, N. E. B. Killeen, P. Raniga, O. Kaluza, A. Ng, G. Poudel, D. Barnes, T. Nguyen, P. Bonnington and G. F. Egan, *Frontiers in Neuroinformatics*, 2014, **8**, 30.
7. A. M. Maiden and J. M. Rodenburg, *Ultramicroscopy*, 2009, **109**, 1256-1262.
8. Y. S. G. Nashed, D. J. Vine, T. Peterka, J. Deng, R. Ross and C. Jacobsen, *Optics Express*, 2014, **22**, 32082-32097.
9. S. Preibisch, S. Saalfeld and P. Tomancak, *Bioinformatics*, 2009, **25**, 1463-1463.
10. J. Schindelin, I. Arganda-Carreras, E. Frise, V. Kaynig, M. Longair, T. Pietzsch, S. Preibisch, C. Rueden, S. Saalfeld, B. Schmid, J.-Y. Tinevez, D. J. White, V. Hartenstein, K. Eliceiri, P. Tomancak and A. Cardona, *Nature Methods*, 2012, **9**, 676-682.
11. C. G. Ryan and D. N. Jamieson, *Nuclear Instruments and Methods in Physics Research B*, 1993, **77**, 203-214.
12. MATLAB, *Image Processing Toolbox*, The MathWorks Inc., Natick, Massachusetts, 2017a.
13. M. van Heel and M. Schatz, *Journal of Structural Biology*, 2005, **151**, 250-262.
14. J. Deng, Y. S. G. Nashed, S. Chen, N. W. Phillips, T. Peterka, R. Ross, S. Vogt, C. Jacobsen and D. J. Vine, *Optics Express*, 2015, **23**, 5438-5451.
15. P. M. Pelz, M. Guizar-Sicairos, P. Thibault, I. Johnson, M. Holler and A. Menzel, *Applied Physics Letters*, 2014, **105**, 251101.
16. J. N. Clark, X. Huang, R. J. Harder and I. K. Robinson, *Physical Review Letters*, 2014, **112**, 113901.
17. P. Thibault and A. Menzel, *Nature*, 2013, **494**, 68-71.